Philosophical Magazine,
Vol. 87, Nos. 8–9, 11–21 March 2007, 1327–1347

Experimental characterization of the mesoscale dislocation density tensor

B. C. LARSON*†, ANTER EL-AZAB‡, WENGE YANG§, J. Z. TISCHLER†, WENJUN LIU¶ and G. E. ICE†

†Materials Science and Technology Division, Oak Ridge National Laboratory, Oak Ridge, TN 37831, USA
‡Mechanical Engineering Department, FAMU-FSU College of Engineering, Florida State University, Tallahassee, FL 32310, USA
§HPCAT/Carnegie Institution of Washington, Advanced Photon Source, Argonne National Laboratory, Argonne, IL 60439, USA
¶XOR/UNI, Advanced Photon Source, Argonne National Laboratory, Argonne, IL 60439, USA

(*Received 22 May 2006; in final form 1 August 2006*)

The dislocation density tensor has been an important variable in the theoretical characterization of dislocations in deformed crystals since its introduction over 5 decades ago. However, the non-destructive, three-dimensional (3D) measurements of lattice rotations and elastic strain needed to determine dislocation density tensors with micron spatial resolution over mesoscopic length scales have until now not been available. We have used 3D X-ray microscopy with sub-micron point-to-point spatial resolution to demonstrate 3D, spatially resolved measurements of the dislocation density tensor in elastically and plastically deformed silicon single crystal plates. Measurements were made of the dislocation density tensor along a line in a ~35 μm thick silicon plate that was bent (elastically) to a 5.42 mm radius of curvature at room temperature, and in a similar sample deformed plastically by annealing to 700°C under bending stress. We discuss the theoretical background for the dislocation density tensor with respect to lattice rotation and elastic strain, we describe the X-ray microscopy technique used to make non-destructive measurement of local rotations and elastic strains with sub-micron resolution in 3D, and we discuss the analysis procedures for extracting dislocation tensors on mesoscopic length scales.

Downloaded By: [Oak Ridge National Laboratory] At: 20:52 4 September 2009

1. Introduction

The present communication presents the theoretical basis for the use of X-ray microscopy to conduct spatially resolved measurements of the dislocation density tensor in plastically deformed crystals and reports recent progress in applying the overall approach to deformed single crystal silicon. Crystal plasticity proceeds by the motion and interaction of dislocations under the influence of the applied stress. During deformation, the dislocation density increases and dislocations are organized

*Corresponding author. Email: bcl@ornl.gov

Philosophical Magazine
ISSN 1478–6435 print/ISSN 1478–6443 online © 2007 Taylor & Francis
http://www.tandf.co.uk/journals
DOI: 10.1080/14786430600943930

into heterogeneous structures that determine the response of the crystal to the applied load [1, 2]. An important aspect of the heterogeneity of the dislocation density in deforming crystals is that the geometric measure of the dislocation density in the crystal becomes nontrivial; this gives rise to lattice curvature and, in turn, the lattice orientation changes from one point to the next, which is a well-studied aspect of plastic deformation of single crystals [3–5]. The relationship between the geometric measure of the dislocation density in distorted crystals and its curvature has been studied for over 50 years [6]. In the early work, what is now called the Nye dislocation density tensor $\boldsymbol{\alpha}$ was introduced. Ignoring the elastic strain in deformed crystals (e.g. in ductile materials) and considering the deformation to be infinitesimal, Nye's tensor is connected with the lattice curvature tensor $\boldsymbol{\kappa}$ by:

$$\boldsymbol{\alpha} = \boldsymbol{\kappa}^{\mathrm{T}} - (\mathrm{tr}\,\boldsymbol{\kappa})\mathbf{I} \quad \text{with inverse} \quad \boldsymbol{\kappa} = \boldsymbol{\alpha}^{\mathrm{T}} - \frac{1}{2}(\mathrm{tr}\,\boldsymbol{\alpha})\mathbf{I}, \tag{1}$$

where $\boldsymbol{\kappa}^{\mathrm{T}}$ and $\mathrm{tr}\,\boldsymbol{\kappa}$ are, respectively, the transpose and trace of the tensor $\boldsymbol{\kappa}$, with similar meaning for $\boldsymbol{\alpha}$, and $\mathbf{I}$ is the identity tensor. Considering infinitesimal crystal distortion, Kröner [7] later developed a continuum theory of dislocations in which the equivalence between the elastic and plastic measures of the dislocation density tensor is demonstrated. This theory incorporates the contribution of the infinitesimal elastic strain tensor $\boldsymbol{\varepsilon}$ to the curvature, yielding the following modification of equation (1):

$$\boldsymbol{\alpha} = \boldsymbol{\kappa}^{\mathrm{T}} - (\mathrm{tr}\,\boldsymbol{\kappa})\mathbf{I} - \nabla \times \boldsymbol{\varepsilon} \quad \text{with inverse} \quad \boldsymbol{\kappa} = \boldsymbol{\alpha}^{\mathrm{T}} - \frac{1}{2}(\mathrm{tr}\,\boldsymbol{\alpha})\mathbf{I} - \boldsymbol{\varepsilon} \times \nabla, \tag{2}$$

with $\mathrm{e}_{\mathrm{ijk}}$ being the permutation symbol, $(\nabla \times \boldsymbol{\varepsilon})_{\mathrm{ij}} = \mathrm{e}_{\mathrm{ikl}}\partial_{\mathrm{k}}\varepsilon_{\mathrm{lj}}$ and $(\boldsymbol{\varepsilon} \times \nabla)_{\mathrm{ij}} = -\mathrm{e}_{\mathrm{jkl}}\partial_{\mathrm{k}}\varepsilon_{\mathrm{li}}$. The curvature tensor gives the incremental change $\mathrm{d}\boldsymbol{\theta}$ in the lattice orientation along a material element $\mathrm{d}\mathbf{x}$ by the formula: $\mathrm{d}\boldsymbol{\theta} = \mathrm{d}\mathbf{x}\cdot\boldsymbol{\kappa}$. Equations (1) and (2) give the direct relationship between the dislocation density tensor and lattice misorientation arising during the plastic distortion of crystals. Under many experimental situations, the lattice misorientation and, in turn, the dislocation density tensor are highly heterogeneous. This heterogeneity is the basis for grain refinement in metals and alloys during thermo-mechanical processing, which underlines the technological importance of understanding the evolution of the dislocation density tensor in deformed crystals.

The concepts of differential geometry were also used to describe the dislocations in crystals [8–10], where a dislocation density measure was defined in the form of a third rank tensor that is equivalently represented by its axial second rank tensor. Since then, many publications defining the dislocation density tensor have appeared that give different measures of the dislocation density tensor at finite deformation. These studies have been critically reviewed in a recent publication by Cermelli and Gurtin [11] who introduced an invariant definition of the dislocation density tensor in the case of finite deformation and offered a consistent physical interpretation of the dislocation tensor in the deformed and reference crystal configurations. These authors also derived evolution equations for the dislocation density tensor and introduced a canonical decomposition that provides a basis for interpreting its components.

The dislocation density tensor has gained further attention lately, being currently used in gradient theories to provide a measure of intrinsic length scale and to capture

Downloaded By: [Oak Ridge National Laboratory] At: 20:52 4 September 2009

the correct hardening behaviour of crystals [12, 13]. In the theory of small deformation, it has been demonstrated that the dislocation density tensor can be used to solve the internal stress boundary value problem associated with dislocations and to capture the long-range stress field of dislocations. The earliest study in that direction has been in the celebrated incompatibility theory of Kröner [7], which was later followed by the Green's function representation of the stress field of continuum density of dislocations by other authors [14, 15]. The long-range stress field of dislocation structures captures the elastic interactions between dislocations, which is known to be a key factor in the kinetics of plastic deformation.

The versatility of the dislocation density tensor in characterizing plastic distortion effects in crystals, as well as its use as a field and constitutive variable in the modern theory of crystal plasticity, makes it important to be able to measure the dislocation tensor experimentally. Electron microscopy has long been used to infer information on dislocation tensors on microscopic length scales [1, 5]. Sub-micron resolution three-dimensional X-ray microscopy only now provides non-destructive, spatially-resolved measurements of local lattice orientations and strain tensors on the critical mesoscopic length scales of the microstructure of materials (i.e. hundreds of nanometres to hundreds of microns) [16–18]. Detailed microstructure and evolution information of this nature provides a quantitative – and previously missing – link between mesoscale deformation in real materials and the results of computer simulations and multi-scale modelling.

The present paper summarizes recent developments in the use of X-ray microscopy to conduct 3D, spatially resolved measurements of the lattice orientation, elastic strain and the dislocation density tensor in plastically deformed crystals. The theoretical basis for measuring the dislocation density tensor is presented in section 2, starting with a summary of the kinematic relationships leading to a definition of the dislocation density tensor and its relationship with the lattice orientation. The equivalence of the elastic and plastic measures of the dislocation density tensor, as given by Cermelli and Gurtin [11], is emphasized for the case of finite deformation. In section 3, recently developed 3D X-ray microscopy techniques capable of investigating the local orientation, phase, microstructure and elastic/plastic strain in deformed materials are discussed. Three-dimensional spatially resolved measurements of the dislocation density tensor are presented for the cases of elastic and plastic bending of thin, single-crystal silicon plates. The paper concludes with comments on the use of dislocation density tensor measurements for direct and quantitative comparisons between X-ray microscopy measurements and computer simulations of deformation processes at the mesoscale.

2. Theoretical foundation

2.1. *Deformation kinematics and definition of the dislocation density tensor*

The deformation of a crystal from a reference configuration $\mathfrak{B}_o$ to a deformed state $\mathfrak{B}_t$ is described by the time-parameterized mapping, where $\mathbf{x} = \boldsymbol{\chi}(\mathbf{X}, t)$ where $\mathbf{x} \in \mathfrak{B}_t$ and $\mathbf{X} \in \mathfrak{B}_o$ are the set of all points in the deformed and reference configurations of

Downloaded By: [Oak Ridge National Laboratory] At: 20:52 4 September 2009

the crystal, respectively. The deformation gradient is defined by $\mathbf{F} = \partial\boldsymbol{\chi}(\mathbf{X},t)/\partial\mathbf{X}$, which, according to Kröner [19] and Lee [20], can be expressed by the multiplicative decomposition:

$$\mathbf{F} = \mathbf{F}^{e}\mathbf{F}^{p}. \tag{3}$$

This decomposition implies that there is an intermediate configuration of the crystal reached from the initial state $\mathfrak{B}_o$ through pure plastic distortion $\mathbf{F}^p$, and from which the deformed (current) configuration $\mathfrak{B}_t$ is reached through pure elastic distortion $\mathbf{F}^e$. This deformation scenario is schematically shown in figure 1, which, along with definition (3), implies that a length element $d\mathbf{X}$ in the reference configuration is mapped onto element $d\mathbf{L}$ in the intermediate configuration, also called the microstructure or lattice configuration, by $d\mathbf{L} = \mathbf{F}^p d\mathbf{X}$. Similarly, element $d\mathbf{L}$ in the intermediate configuration is mapped onto $d\mathbf{X}$ in the deformed configuration by $d\mathbf{X} = \mathbf{F}^e d\mathbf{L}$. The discussion here is confined to cases in which $\mathbf{F}^p$ represents pure crystallographic slip by dislocation glide with no change in lattice orientation. The polar decomposition theorem allows us to express $\mathbf{F}^e$ and $\mathbf{F}^p$ in the form:

$$\mathbf{F}^{e} = \mathbf{R}^{e}\mathbf{U}^{e} = \mathbf{V}^{e}\mathbf{R}^{e} \text{ and } \mathbf{F}^{p} = \mathbf{R}^{p}\mathbf{U}^{p} = \mathbf{V}^{p}\mathbf{R}^{p}, \tag{4}$$

where $\mathbf{R}^e$ and $\mathbf{R}^p$ are, respectively, the elastic and plastic rotations, $\mathbf{U}^e$ and $\mathbf{U}^p$ the elastic and plastic right-stretch tensors, and $\mathbf{V}^e$ and $\mathbf{V}^p$ the elastic and plastic left-stretch tensors. In the case of dislocation glide, the plastic distortion tensor is given by:

$$\mathbf{F}^{p} = \mathbf{I} + \sum_{\alpha=1}^{A} \gamma^{\alpha}\mathbf{s}^{\alpha} \otimes \mathbf{m}^{\alpha} \tag{5}$$

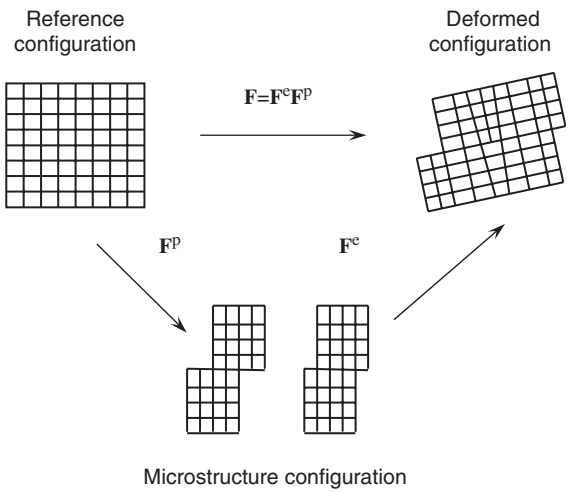

Figure 1. Schematic illustration of multiplicative decomposition of the deformation gradient.

Downloaded By: [Oak Ridge National Laboratory] At: 20:52 4 September 2009

in which γ^α is the shear strain on the αth slip system, which has slip direction and slip plane normal defined by $\mathbf{s}^\alpha$ and $\mathbf{m}^\alpha$, respectively; A is the number of slip systems. The time rate of change of $\mathbf{F}^{\mathrm{p}}$ is given by:

$$\dot{\mathbf{F}}^{\mathrm{p}} = \mathbf{L}^{\mathrm{p}}\mathbf{F}^{\mathrm{p}} \quad \text{with } \mathbf{L}^{\mathrm{p}} = \sum_{\alpha=1}^{\mathrm{A}} \dot{\gamma}^\alpha \mathbf{s}^\alpha \otimes \mathbf{m}^\alpha, \tag{6}$$

where γ^α is the shear strain rate on the αth slip system. In the case of dislocation glide trace $(\mathbf{L}^{\mathrm{p}}) = 0$ and $\mathrm{J}^{\mathrm{p}} = \det(\mathbf{F}^{\mathrm{p}}) = 1$, implying that the plastic distortion is isochoric.

Following Cermelli and Gurtin [11], there is an invariant measure of the dislocation density tensor defined in the intermediate configuration of the crystal by:

$$\boldsymbol{\alpha}_{\mathrm{L}} = \mathrm{J}^{\mathrm{p}-1}\mathbf{F}^{\mathrm{p}}\,\mathrm{CURL}\,\mathbf{F}^{\mathrm{p}} = \mathrm{J}^{\mathrm{e}}\mathbf{F}^{\mathrm{e}-1}\mathrm{curl}\,\mathbf{F}^{\mathrm{e}-1}, \tag{7}$$

in which $\mathrm{J}^{\mathrm{e}} = \det(\mathbf{F}^{\mathrm{e}})$, and CURL and curl are the curl operators in the reference and deformed configurations, respectively. Equation (7) asserts the equivalence between the elastic and plastic measures of the dislocation density tensor in deforming crystals. Standard pullback and push forward operations of the dislocation density tensor in the lattice configuration give their counterparts in the reference and deformed crystal configurations, respectively, by:

$$\boldsymbol{\alpha}_{\mathrm{R}} = \mathrm{J}^{\mathrm{p}}\mathbf{F}^{\mathrm{p}-1}\boldsymbol{\alpha}_{\mathrm{L}}\mathbf{F}^{\mathrm{p}-\mathrm{T}} = (\mathrm{CURL}\,\mathbf{F}^{\mathrm{p}})\mathbf{F}^{\mathrm{P}-\mathrm{T}} \quad \text{and} \quad \boldsymbol{\alpha} = \mathrm{J}^{\mathrm{e}-1}\mathbf{F}^{\mathrm{e}}\boldsymbol{\alpha}_{\mathrm{L}}\mathbf{F}^{\mathrm{eT}} = (\mathrm{curl}\,\mathbf{F}^{\mathrm{e}-1})\mathbf{F}^{\mathrm{eT}}. \tag{8}$$

These two dislocation density measures are connected by $\boldsymbol{\alpha}_{\mathrm{R}} = \mathrm{J}\mathbf{F}^{-1}\boldsymbol{\alpha}\mathbf{F}^{-\mathrm{T}}$, with $\mathbf{F}^{-1}$ being the inverse of $\mathbf{F}$, $\mathbf{F}^{-\mathrm{T}}$ the transpose of $\mathbf{F}^{-1}$, and $\mathrm{J} = \det(\mathbf{F}) = \det(\mathbf{F}^{\mathrm{e}})$.

2.2. *Theoretical basis of dislocation density tensor measurements*

The above definition of the dislocation density tensor will now be used to outline the theoretical basis for the X-ray technique presented in section 3 for measuring the dislocation density tensor. As this task proceeds, it is useful to keep the following general considerations in mind: (1) the dislocation density tensor has two equivalent definitions, one in terms of the plastic distortion field and another in terms of the elastic distortion field; (2) the process of crystal deformation leaves behind three signatures – lattice curvature (in the sense of changes in the lattice orientation over differential length elements), lattice elastic strain (in the sense of distorted Bravais unit cells of the crystal relative to its stress free state), and lattice dislocations (defects) with variable densities in the crystal; (3) it is not possible to use these three signatures to reconstruct the plastic distortion field in the crystal because a dislocation density tensor field does not give rise to a unique plastic distortion field, although the opposite is true; (4) the lattice curvatures, strains and dislocation densities can only be measured in the deformed (i.e. physical or current) crystal configuration; and, finally, (5) the information on lattice rotation and stretching within the crystal resides in the elastic rotation and stretch tensors.

The X-ray microscopy technique presented in section 3 is based on the above considerations in the sense that X-ray microscopy provides a measure of the dislocation density tensor via spatially resolved measurement of local lattice

Downloaded By: [Oak Ridge National Laboratory] At: 20:52 4 September 2009

orientation and elastic strain, both components of the elastic distortion field $\mathbf{F}^e$ in the crystal. The theoretical basis of the technique, thus, starts out with the definition of the dislocation density tensor in terms of elastic distortion. Associated with this definition are two relationships: $\boldsymbol{\alpha} = (\mathrm{curl}\,\mathbf{F}^{e-1})\mathbf{F}^{eT}$, see equation (8), and $\mathbf{F}^e = \mathbf{R}^e\mathbf{U}^e = \mathbf{V}^e\mathbf{R}^e$, see equation (4). We note here that any lattice vector, such as the lattice translation vectors, remains invariant following the plastic distortion step. It is during the elastic distortion that these vectors are stretched and/or rotated. In other words, $\mathbf{F}^e$, or alternatively its components $\mathbf{R}^e$ and $\mathbf{U}^e$ (or $\mathbf{V}^e$), quantify the transformation of the lattice vectors from the intermediate crystal configuration to its final (deformed) configuration. These considerations are important in the interpretation of X-ray microscopy data and lead to the four special cases discussed below: finite elastic distortion, finite rotation with infinitesimal elastic strain, infinitesimal elastic distortion and infinitesimal distortion.

Downloaded By: [Oak Ridge National Laboratory] At: 20:52 4 September 2009

2.2.1. Finite elastic distortion. Let the lattice rotation be expressed in terms of the vector $\boldsymbol{\theta} = \theta\mathbf{w}$ consisting of a rotation angle θ about some orientation defined by the unit vector $\mathbf{w}$. Associated with this rotation is a skew second order tensor $\mathbf{W} = (\boldsymbol{\theta}\times) = \theta(\mathbf{w}\times)$ with the vector $\boldsymbol{\theta}$ being its axial (or dual) vector. In component form, $\mathbf{W}$ and $\theta\mathbf{w}$ are related by $\mathrm{W_{ij}} = \mathrm{e_{ijk}}\theta\mathrm{w_k}$. The rotation tensor $\mathbf{R}^e$ is defined by the exponential of the tensor $\mathbf{W} = (\boldsymbol{\theta}\times)$:

$$\mathbf{R}^e = \exp(\mathbf{W}) = \sum_{\mathrm{k}=0}^{\infty} \frac{1}{\mathrm{k}!}\mathbf{W}^{\mathrm{k}} = \cos\theta\,\mathbf{I} + \sin\theta\,(\mathbf{w}\times) + (1-\cos\theta)\,\mathbf{w}\otimes\mathbf{w}, \tag{9}$$

where $\mathbf{w}\otimes\mathbf{w}$ is the tensor product of $\mathbf{w}$ with itself. Component-wise, the above relationship is written in the form:

$$\mathrm{R^e_{ij}} = \cos\theta\delta_{\mathrm{ij}} - \sin\theta\mathrm{e_{ijk}}\mathrm{w_k} + (1-\cos\theta)\mathrm{w_i}\mathrm{w_j}, \tag{10}$$

with δ_{ij} being the Kronecker delta. On the other hand, the right-hand stretch tensor $\mathbf{U}^e$ is defined in terms of the finite, symmetric lattice strain tensor $\mathbf{E}$ by the relationship:

$$\mathbf{U}^e = \sqrt{\mathbf{I} + 2\mathbf{E}}, \tag{11}$$

where the positive definite square root is considered. Experimental measurement of the dislocation density tensor then proceeds as follows: spatially resolved measurements of the vector $\boldsymbol{\theta} = \theta\mathbf{w}$ and the strain tensor $\mathbf{E}$ are performed, from which the spatially resolved values of the rotation and the right-stretch tensors are constructed. This leads to a point-to-point construction of the elastic distortion tensor. The definition $\boldsymbol{\alpha} = (\mathrm{curl}\,\mathbf{F}^{e-1})\,\mathbf{F}^{eT}$ is then used to construct the dislocation density tensor in the deformed crystal configuration. The pullback operations $\boldsymbol{\alpha}_R = \mathrm{J}\mathbf{F}^{-1}\boldsymbol{\alpha}\mathbf{F}^{-T}$ can be applied to recover the dislocation density tensor in the reference configuration.

Downloaded By: [Oak Ridge National Laboratory] At: 20:52 4 September 2009

2.2.2. Finite rotation with infinitesimal elastic strain. In this case, the right-stretch tensor is approximately equal to the identity tensor and the elastic distortion tensor is approximated by the elastic rotation tensor. That is:

$$\mathbf{U}^{\mathrm{e}} \approx \mathbf{I} \text{ and } \mathbf{F}^{\mathrm{e}} \approx \mathbf{R}^{\mathrm{e}}. \tag{12}$$

This approximation is known as the elastically rigid plastic approximation, where the inhomogeneous plastic distortion of the lattice is fully accommodated by the elastic lattice rotation alone. The expression of the dislocation density tensor is rewritten in the form:

$$\boldsymbol{\alpha} = (\mathrm{curl}\,\mathbf{R}^{\mathrm{eT}})\mathbf{R}^{\mathrm{eT}}, \tag{13}$$

where use has been made of the fact that $\mathbf{R}^{\mathrm{e}-1} = \mathbf{R}^{\mathrm{eT}}$, a property of the orthogonal tensor $\mathbf{R}^{\mathrm{e}}$. Measurement of the dislocation density tensor when elastic strain is negligible is straightforward: it is only necessary to perform spatially resolved measurements of the vector $\boldsymbol{\theta} = \theta\mathbf{w}$, from which the spatially resolved rotation tensor is constructed directly. This leads to a point-to-point construction of dislocation density tensor according to equation (13). Again, this gives the dislocation density tensor in the deformed configuration, which can be pulled back to the reference configuration as given previously.

2.2.3. Infinitesimal elastic distortion. In the case of infinitesimal elastic distortion, it is easy to show that the following equations hold:

$$\left.\begin{aligned} \mathbf{U}^{\mathrm{e}} &\approx \mathbf{I} + \mathbf{E} + \cdots \\ \mathbf{R}^{\mathrm{e}} &\approx \mathbf{I} + \mathbf{W} + \cdots \\ \mathbf{F}^{\mathrm{e}} &\approx \mathbf{I} + (\mathbf{W} + \mathbf{E}) + \cdots \\ \mathbf{F}^{\mathrm{e}-1} &\approx \mathbf{I} - (\mathbf{W} + \mathbf{E}) + \cdots \end{aligned}\right\} \text{ with higher order terms omitted} \tag{14}$$

The notation of Kröner [7] can now be established by defining the elastic part of the displacement gradient $\boldsymbol{\beta}^{\mathrm{e}}$ in the infinitesimal elastic distortion case by $\boldsymbol{\beta}^{\mathrm{e}} = \mathbf{W} + \mathbf{E}$, so that $\mathbf{F}^{\mathrm{e}-1} \approx \mathbf{I} - \boldsymbol{\beta}^{\mathrm{e}}$, which gives:

$$\boldsymbol{\alpha} \approx [\mathrm{curl}\,(\mathbf{I} - \boldsymbol{\beta}^{\mathrm{e}})](\mathbf{I} - \boldsymbol{\beta}^{\mathrm{e}}) \approx -\mathrm{curl}\,\boldsymbol{\beta}^{\mathrm{e}}. \tag{15}$$

Again, higher order terms have been omitted in reaching the final expression. To arrive at the results in (14), the summation in equation (9) has been truncated beyond the first order. The skew tensor $\mathbf{W}$ is called the infinitesimal rotation tensor; it is the skew (anti-symmetric) part of $\boldsymbol{\beta}^{\mathrm{e}}$. Also, the strain tensor $\mathbf{E}$ in this case reduces to the infinitesimal elastic strain tensor $\boldsymbol{\varepsilon}$, which is the symmetric part of $\boldsymbol{\beta}^{\mathrm{e}}$. Equation (15) is consistent with Kröner's development of the theory of internal stresses starting from the assumption of additive decomposition of the displacement gradient in terms of the infinitesimal elastic and plastic distortions [7]. However, we emphasize here that this result is valid regardless of the magnitude of the plastic distortion. In other words, although it has been assumed that the elastic distortion is infinitesimal, this

result does not mean that the distinction between the reference and deformed configurations of the crystal is completely discarded because the plastic distortion can still be finite.

The procedure for measuring the dislocation density tensor in the deformed crystal configuration is as follows: conduct spatially resolved measurements of the infinitesimal rotation vector $\boldsymbol{\theta} = \theta \mathbf{w}$, from which the spatially resolved infinitesimal rotation tensor $\mathbf{W}$ is constructed. This, along with the infinitesimal elastic strain tensor, leads to a point-to-point construction of the dislocation density tensor according to equation (15). Again, this gives the dislocation density tensor in the deformed configuration.

2.2.4. Infinitesimal deformation. The expression of the dislocation density tensor in section 2.2.3 and the procedure for measurement of the dislocation density tensor remain essentially valid in the case of infinitesimal deformation, with one further consideration: the dislocation densities in the deformed crystal configuration, the lattice configuration and the reference configuration are the same.

Downloaded By: [Oak Ridge National Laboratory] At: 20:52 4 September 2009

3. Characterization of the dislocation density tensor

As emphasized above, the dislocation tensor defined in equations (1) and (2) in terms of lattice curvature and strain gradients is an inherently local quantity requiring 3D spatially resolved crystallographic orientation and elastic strain measurements for its specification. The penetrating power of hard X-rays (>5 keV) provides nondestructive diffraction measurements in the interior of materials inherently; until recently though, the needed spatial resolution in 3D has been missing. However, with the development of high-brilliance, third generation synchrotron X-ray sources, the availability of precision, hard X-ray, focusing mirrors and the development of submicron resolution depth profiling techniques, the 3D spatially-resolved capabilities needed to extract local crystallographic orientations, orientation gradients and strain have now become a reality. Below, we discuss the submicron resolution 3D X-ray microscopy technique briefly, indicate the method for performing 3D measurements of lattice curvature and strain tensors, and provide direct measurements of the dislocation tensors for the cases of elastically and plastically bend-deformed silicon.

3.1. *Three-dimensional X-ray microscopy*

Submicron diameter beams of polychromatic X-rays produced by high-precision, elliptically figured X-ray focusing mirrors have been available for some time for performing 2D X-ray structural microscopy [21–23]. Figure 2 depicts schematically the depth profiling extension of 2D X-ray microscopy that enables submicron resolution X-ray microscopy measurements in three-dimensions. The ability to choose polychromatic or monochromatic incident X-ray beams and the focusing of the beam by crossed Kirkpatrick–Baez X-ray mirrors is shown. With the sample

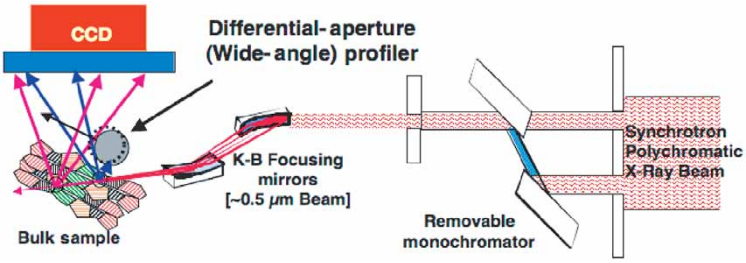

Figure 2. Schematic drawing of the 3D X-ray microscope facility on the XOR/UNI Sector 34 beamline at the Advanced Photon Source. The incident polychromatic undulator X-ray beam, the insertable double crystal monochromator and Kirpatrick–Baez focusing mirrors are all shown. The sample diffracts white (polychromatic) X-rays into the CCD area detector from along the microbeam. The 50 μm diameter Pt wire (knife-edge) profiler provides submicron depth resolution along the microbeam.

Downloaded By: [Oak Ridge National Laboratory] At: 20:52 4 September 2009

placed at the focal point of the mirrors, polychromatic or monochromatic diffraction patterns are collected on a charge-coupled device (CCD) area detector. The critical aspect for 3D microscopy is the inclusion of a 50 μm differential aperture (i.e. knife-edge) platinum wire that functions as a knife-edge depth profiler.

As discussed in detail elsewhere [16, 17, 24] submicron-resolution depth-resolved X-ray diffraction patterns are extracted from the measurements by collecting polychromatic (white) beam diffraction patterns on the CCD as the profiling wire is step-scanned through the diffracted beams, sequentially occluding scattering from each depth and scattering angle. Computer collation and geometrical triangulation analysis (performed on differences between images taken before and after successive profiler steps) generates the source position along the microbeam of all diffracted intensities on the CCD. Noting that the profiling wire is much closer (typically <200 μm) to the sample than to the 24 μm square CCD pixels (located ~40 mm from the sample), less than ~0.1 μm parallax is generated by the finite pixel sizes. This makes the depth resolution largely a function of the wire step size. Calibration and alignment of the X-ray microscopy system is performed by measurements on a thin 4 μm thick, single-crystal Si plate [25].

The origin along the microbeam of the intensity in individual pixels in the CCD is determined by triangulating from the pixel position to the wire position and then extrapolating to the position along the microbeam. Repeating this process for each pixel and each step of the profiler wire makes it possible to reconstruct computationally, full diffraction patterns from submicron increments along the microbeam penetration direction. The extraction of full Laue diffraction patterns from submicron voxels is the fundamental basis of this X-ray microscopy technique – full diffraction patterns imply the potential for obtaining full diffraction information from each voxel on a point-to-point basis along the microbeam.

Each scan of the wire across the diffracted beams provides depth-resolved measurements along the line of the microbeam in the sample; therefore, by rastering the microbeam over a two-dimensional array in a stepwise fashion and performing depth resolved measurements at each point of the rastered 2D array, 3D arrays of diffraction patterns can be generated. As discussed by Yang *et al.* [25], depth

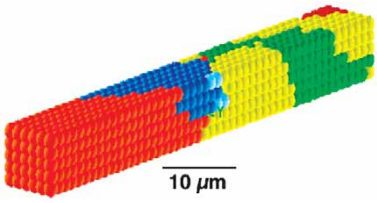

Figure 3. False-colour, 3D X-ray microscopy image of polycrystalline grain structure in aluminium, where the 1 μm cubed voxel sizes illustrate the spatial resolution.

Downloaded By: [Oak Ridge National Laboratory] At: 20:52 4 September 2009

profiling scans requires 300–400 profiler steps (20–30 min) to transit the entire CCD for each point of the 2D area scan. Although scanning techniques are intrinsically slow compared to full-field measurements, at present it is the only technique providing the submicron, point-to-point spatial resolution needed for dislocation tensor measurements. It provides nondestructive measurements of crystal structure, crystal orientation, and elastic strain tensor measurements along the microbeam, thus making it possible to determine the local structure, orientation, and both plastic and elastic strain tensors with micron or submicron spatial resolution over 3D arrays. It should be mentioned that a much faster, high-energy, monochromatic beam 3D X-ray microscope technique exists, which employs sample rotations to probe individual grain orientations or deformed regions in crystalline materials. So far, resolution of only a few microns has been demonstrated [26], so, unfortunately, the power and speed of this technique is not applicable for the work discussed in this paper.

An example of the ability to use local orientation measurements to resolve grain boundaries and subgrain microstructure in polycrystalline materials [25] is shown in figure 3. This figure shows a colour-coded 3D image of the local crystallographic orientation, where crystal grains, boundaries and sub-boundaries can be identified with the micron resolution of the measurements. The relevance to deformation investigations is that analogous quantitative, non-destructive microstructural measurements performed on deformed samples make it possible to characterize local lattice microstructure orientations and orientation gradients. 3D arrays of local orientations and orientation gradients, in turn, provide the capability for a direct and absolute comparison of experimental results with computational modelling and with fundamental elasticity/plasticity theory.

Performing local orientation measurements on deformed materials is more difficult than in un-deformed materials, of course. This is due to the quasi-continuous nature of lattice rotations from micron-to-micron within deformation microstructure as compared to abrupt orientation changes (often with little or no rotational deformation) at polycrystal grain boundaries. Nevertheless, elastic strain measurements in cylindrically bent Si plates, which have continuous curvature, were the first submicron resolution 3D strain tensor measurements to be reported [16]. The ability to measure local crystal rotations within the plastic deformation zone under nanoindentations in single crystal Cu [27] has been demonstrated as well.

As discussed below in connection with measurements on both plastically and elastically bent Si, continuous rotations are reflected in terms of streaked diffraction peaks rather than sharp, round diffraction spots. Therefore, as will be evidenced below, continuous distortions impact the precision with which local orientations and elastic strains can be determined, depending on the spatial resolution of the measurement, but they do not preclude such measurements in general.

3.2. *Measurement of lattice orientations and strain in deformed crystals*

The two limiting cases of fully elastic distortion ($\mathbf{F}^{\mathrm{P}} = \mathrm{I}$) and elastically rigid plastic distortion (no lattice strain) correspond to equations (11) and (12), respectively. The first case is readily achievable in brittle materials such as Si at room temperature, even for relatively large strains. The second case of stress-free plastic distortions is not fully achievable even in ductile materials, but such conditions are approximated in ductile materials at low deformation levels. To demonstrate mesoscale dislocation tensor measurement and analysis techniques using X-ray microscopy in this paper, we utilize both elastic and plastic deformation in cylindrically bent Si. This serves as a test of the ability of 3D X-ray microscopy to measure dislocation tensors on mesoscopic length scales in connection with equations (1) and (2).

Since Si is brittle at room temperature, but begins to deform plastically above ~625°C, it is possible to cylindrically deform Si completely elastically at room temperature and it is possible to deform it (at least partially) plastically by heating it above 625°C under bending strain and cooling to room temperature for lattice curvature and strain measurements. These two conditions are used here to provide access to widely differing (elastic versus plastic) strain states on which dislocation tensor measurements can be performed.

Measurements were performed on ~2-mm wide Si strips scribed and cleaved from commercially available ~35-μm thick ⟨100⟩ surface normal Si wafers. Several such Si strips were bent (elastically) into the shape of arches at room temperature and maintained in this configuration by constraining their ends within a 12.5-mm wide slot in a quartz microscope slide, as shown in figure 4a. For the ~13–14-mm long strips used, this resulted in ~5–6-mm radii of curvature at the apex of the arches, where the radius of curvature was determined directly by microbeam measurements performed in the geometry depicted in figure 4a. The use of a quartz holder made it possible to heat the elastically bent samples to 700°C. This procedure introduced dislocations in a semi-controlled manner as shown in figure 4b, where the elastic stresses lead to an approximately cylindrical plastic deformation, which can be seen to be concentrated most heavily at the apex of the arch. The presence of plastic deformation induced by annealing under a bending stress is additionally evidenced by the optical microscope observations of slip traces on the sample surface in figure 4c, as well as directly by the microbeam measurements discussed below. The y-axis direction is vertical in figure 4c and perpendicular to the slip-traces.

Figures 4d–f show the Si (00L) Laue diffraction spots as measured on the CCD camera for three cases. Figure 4d is a uniformly streaked (in both direction and intensity) diffraction spot measured on elastically bent Si at a ~45° angle perpendicular to the bend axis at the arch apex. Figure 4e is a single streak but

Downloaded By: [Oak Ridge National Laboratory] At: 20:52 4 September 2009

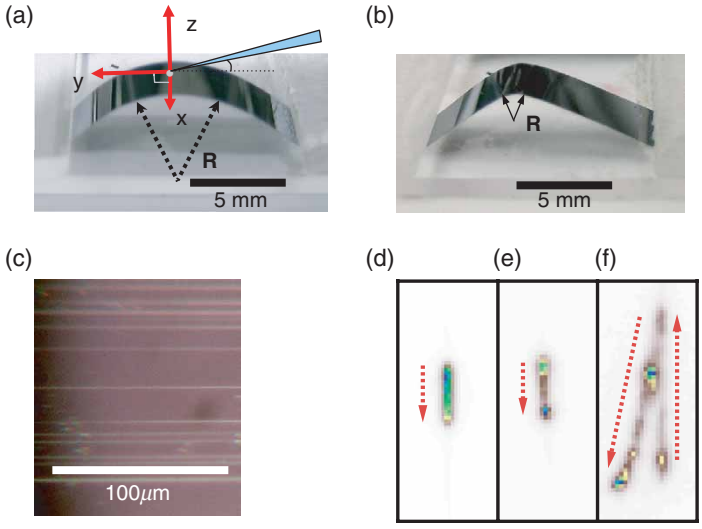

Figure 4. (a) Photograph of a Si plate elastically bent into an arch in a quartz slot before anneal; the microbeam, the bend radius R and the x–y–z axes of the sample are indicated. (b) Photograph of (a) following a 700°C anneal showing plastic bending. (c) Slip traces (perpendicular to the y-direction) on the Si surface after a 700°C anneal under the bending stress in (a). (d) (00L) diffraction streak corresponding to bending around the x-axis in elastically bent Si plate. (e) and (f) (00L) diffraction streaks corresponding to plastic bending (nominally around the x-axis) after a 700°C anneal.

with non-uniform intensity measured on a 700°C annealed sample. Figure 4f is a nonuniform streak (in both direction and intensity) in a particular region found to depart markedly from cylindrical plastic deformation. The uniform diffraction intensity as a function of elongation in the streak for elastically bent Si is an indicator of uniform bending (around the x-axis) with depth, while the non-uniform Laue spots (as in figures 4e and f) are indicators of heterogeneous plastic deformation rotations. In the next section, we present 3D X-ray microscopy measurements of the lattice curvature, elastic and plastic strain gradients, and dislocation tensors under the three conditions of elastic deformation, light plastic deformation, and heavier plastic deformation.

3.3. *Dislocation density tensor measurement*

Figure 5a shows micron resolution local lattice orientation measurements in terms of three orthogonal rotation vectors obtained by 3D X-ray microscopy as a function of distance along the X-ray microbeam as it penetrates through the sample; the beam was incident at 45° at the centre of the cylindrically bent (elastically) Si strip (see figure 4a). The rotation angles are (arbitrarily) referenced to the middle of the sample and the angular range of the diffracted X-rays on the CCD corresponds to the Laue spot in figure 4d. The linear change in θ_x along the microbeam corresponds to a constant curvature with a bend radius of $R = 5.42$ mm. Figure 5b is a plot of the

Downloaded By: [Oak Ridge National Laboratory] At: 20:52 4 September 2009

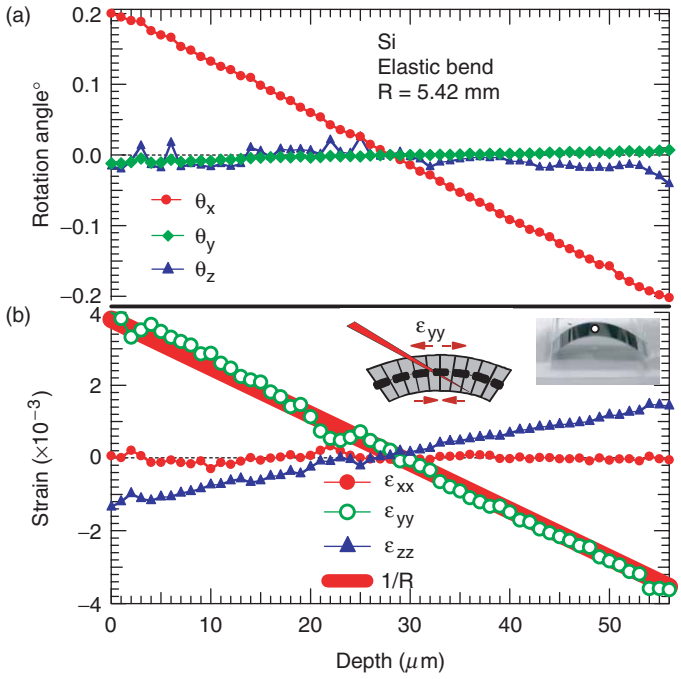

Figure 5. (a) Rotations about the x, y and z directions (see figure 4a) measured along the X-ray microbeam in cylindrically bent Si. (b) Diagonal strain tensor components as a function of depth along the microbeam. The solid red (dark grey) line shows the slope of the slope of ε_{yy} expected for completely elastic bending. The inset depicts schematically the bending induced tension at the top surface, the neutral plane and the compression at the lower surface. For full colour, see on-line.

normal lattice strains as a function of depth along the microbeam. As was done previously [16], these total strain (deviatoric + dilatational) tensor values were obtained from deviatoric strain measurements using the fact that the strain in the x-direction (along the axis of the bend) vanishes by symmetry, because anticlastic bending is suppressed by the cylindrical geometry. If the cylindrical bending is elastic, the radial gradient of the strain along the curved surface (i.e. y-direction) will be given by the inverse of R. Since the thick red line in figure 5b, which corresponds to a slope of $\cos(\pi/4)/(5.42\,\text{mm})$, represents a good fit to the measured slope of ε_{yy} (cylindrical bending strains are illustrated schematically in the inset), we conclude that equation (2) is satisfied with the dislocation tensor $\boldsymbol{\alpha} = \mathbf{0}$, in which case:

$$\nabla\boldsymbol{\theta} - \mathrm{tr}(\nabla\boldsymbol{\theta})\,\mathbf{I} - \nabla \times \boldsymbol{\varepsilon} = \mathbf{0}. \tag{16}$$

Referring to figure 4, the above equation is satisfied by one nontrivial rotation about the out-of-plane axis whose gradient along the sample is equal to the curvature $(1/R)$ in that direction and one strain component ε_{yy} with gradient in the radial direction that is also equal to the sample curvature $1/R$ – here R is the radius of curvature of the sample. We note here that $\boldsymbol{\kappa} = (\nabla\boldsymbol{\theta})^T$. This is, of course, in agreement with the well-known result that at room temperature Si is brittle and bends

Downloaded By: [Oak Ridge National Laboratory] At: 20:52 4 September 2009

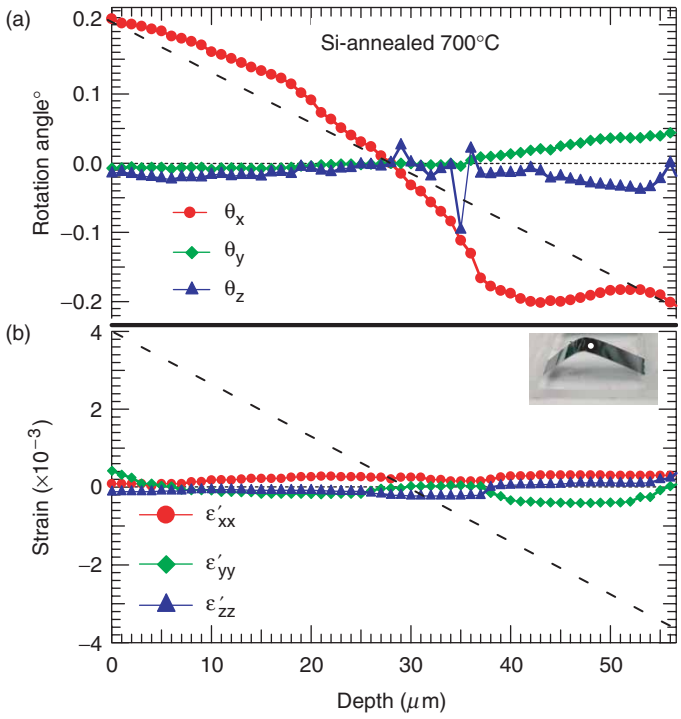

Figure 6. (a) Rotations about the x, y and z directions measured on cylindrically bent Si after a 700°C anneal under bending stress. The dashed line shows the x-axis rotation measured before annealing. (b) Diagonal deviatoric strain components measured after the anneal with the dashed line indicating the strain gradient measured before annealing.

completely elastically. The small deviations of the strain as a function of depth with respect to the slope of the curvature are estimated to be within the (~ 1–2×10^{-4}) uncertainties of the strain measurements for Si without dislocations.

Figures 6a and 7a show analogous local rotation and deviatoric strain measurements made at two positions near the apex of the arch after annealing at 700°C in air for 30 min and slowly cooling (under the bending constraint within the slot). The data in figure 6a correspond to the Laue spot in figure 4e. We note that θ_x in figure 6a, unlike figure 5a, is neither linear nor is it completely monotonic; although it varies relatively smoothly as a function of depth, the slope becomes significantly steeper at $\sim$35 μm and the rotations have increased θ_y and θ_z components beyond 40 μm.

As illustrated by the thick dashed line in figure 6a, the overall rotation of 0.4° is similar in magnitude to that measured for the elastically bent case. On the other hand, the deviatoric strain tensor measurements are of a very different form from those observed for elastically bent Si in figure 5b. All three (diagonal) deviatoric strain components in figure 6b are small and they are essentially flat as a function of depth. This suggests that the elastic bending strains are significantly relaxed by the generation of dislocations during the 700°C anneal; the dashed line in figure 6b indicates the slope of ε_{yy} for elastic bending.

Downloaded By: [Oak Ridge National Laboratory] At: 20:52 4 September 2009

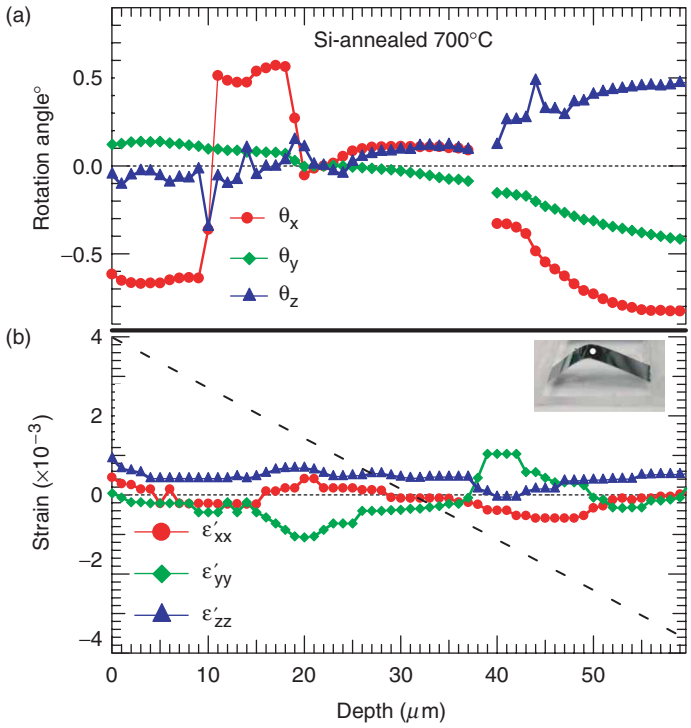

Figure 7. (a) Rotations about the x, y and z directions measured at a second position (as for figure 6a, but at a position with larger and more complex rotations) after a 700°C anneal under bending stress. (b) Diagonal deviatoric strain components measured at the second position after the anneal. The dashed line indicates the strain gradient measured before annealing.

Figure 7a shows the measured angular rotations as a function of depth associated with the fragmented and streaked Laue diffraction pattern in figure 4f at the second position in the 700°C annealed sample. This position was closer to the apex of the arch and selected owing to its (atypical) fragmented Laue diffraction pattern and its larger curvature than at the figure 4e position. As indicated by θ_x, θ_y, and θ_z in figure 7a, both positive and negative rotations are present at this position. This is consistent with the directional arrows in figure 4f denoting the diffraction pattern progression as a function of depth along the microbeam; the discontinuous intensity distribution in figure 4f is a result of the sharp rotational jumps in lattice orientation observed in figure 7a. Note that the angular rotations in figure 7a are plotted on a scale five times larger than in figures 5a and 6a, and that the deviatoric strains in figures 6b and 7b have been median-smoothed to reduce the impact of measurement fluctuations on the strain gradients in figures 8 and 9. Compared to the dashed line denoting the slope for elastically bent Si in figure 5b, the slope of the diagonal deviatoric strains are again small compared to that for elastic bending observed in figure 5b, signifying dislocation induced relaxation. It should be noted that figures 6b and 7b are deviatoric strain tensor components denoted by the 'prime', whereas

Downloaded By: [Oak Ridge National Laboratory] At: 20:52 4 September 2009

figure 5b represents full strain tensor (deviatoric + dilatational) components for the elastic bending case. Although the dilatational strain was not measured for the annealed case, dilatation is assumed to be small considering the flatness of the deviatoric strain tensor with depth compared to the elastic case.

To make the extraction of the dislocation tensor from the measured curvature and strain tensors using equation (2) clear, we write $\alpha_{ij} = \kappa_{ji} - \delta_{ij}\kappa_{kk} - e_{ikl}\partial_k\varepsilon_{lj}$ explicitly as

$$\alpha_{ij} = \begin{pmatrix} \kappa_{11} & \kappa_{21} & \kappa_{31} \\ \kappa_{12} & \kappa_{22} & \kappa_{32} \\ \kappa_{13} & \kappa_{23} & \kappa_{33} \end{pmatrix} - (\kappa_{11} + \kappa_{22} + \kappa_{33}) \begin{pmatrix} 1 & 0 & 0 \\ 0 & 1 & 0 \\ 0 & 0 & 1 \end{pmatrix} - \begin{pmatrix} \varepsilon_{31,2} - \varepsilon_{21,3} & \varepsilon_{32,2} - \varepsilon_{22,3} & \varepsilon_{33,2} - \varepsilon_{23,3} \\ \varepsilon_{11,3} - \varepsilon_{31,1} & \varepsilon_{12,3} - \varepsilon_{32,1} & \varepsilon_{13,3} - \varepsilon_{33,1} \\ \varepsilon_{21,1} - \varepsilon_{11,2} & \varepsilon_{22,1} - \varepsilon_{12,2} & \varepsilon_{23,1} - \varepsilon_{13,2} \end{pmatrix}. \tag{17}$$

where we understand 1, 2, and 3 in the subscripts to correspond to x, y and z in the sample coordinate system. The first and second terms on the right-hand side represent rotational gradients generating dislocation densities while the third term accounts for elastic strain gradients without the generation of dislocations.

Equation (17) emphasizes the need to measure each of the lattice rotation gradients and strain gradients to determine the dislocation density tensor. It further indicates that concluding $\boldsymbol{\alpha} = \mathbf{0}$ for the elastic bending case in figure 5b corresponded to the experimental demonstration that $\kappa_{yx} = \varepsilon_{yy,z} = 1/R$, since they represent the only non-zero components on the right side of equation (17) for cylindrical elastic bending geometry.

Such simple arguments cannot be made for plastic distortions, so each of the components must be determined separately from the measured curvatures and strain tensor values. Since the results in figures 6 and 7 represent measurements along a single line in the sample, they do not provide orientation and strain gradient information perpendicular to the beam direction. Therefore, they do not by themselves provide sufficient 3D information to determine the full curvature and strain gradient tensors. Accordingly, the local rotation and strain measurements were repeated with the sample translated 1 μm in the x-direction and also with the sample translated 1.414 μm in the y-direction. Combining measurements at all three positions in the numerical differentiation process provides the curvature and elastic strain gradient information needed to determine all nine components of $\boldsymbol{\alpha}$ with micron spatial resolution in the x–y–z coordinate system of the sample as defined in figure 4a.

The solid lines in figures 8 and 9 are line plots of the nine components of the curvature part of $\boldsymbol{\alpha}$ given by $\theta_{i,j} - \delta_{ij}\theta_{k,k}$ (measured as a function of position along the beam) and the dotted lines represent the elastic strain part $-\nabla \times \boldsymbol{\varepsilon}$. The open circles in figures 8 and 9 denote the full $\boldsymbol{\kappa}$ tensor. We comment first of all that full-scale of 1.2 mrad/μm in figure 8 corresponds to a rotation of less than 0.06°, so relatively high precision measurements are required and measurement uncertainties and statistical fluctuations can be expected to have an impact. Note the factor of 10 increase in the scale for figure 9 compared to figure 8. Keeping these facts in mind, we focus first on

Downloaded By: [Oak Ridge National Laboratory] At: 20:52 4 September 2009

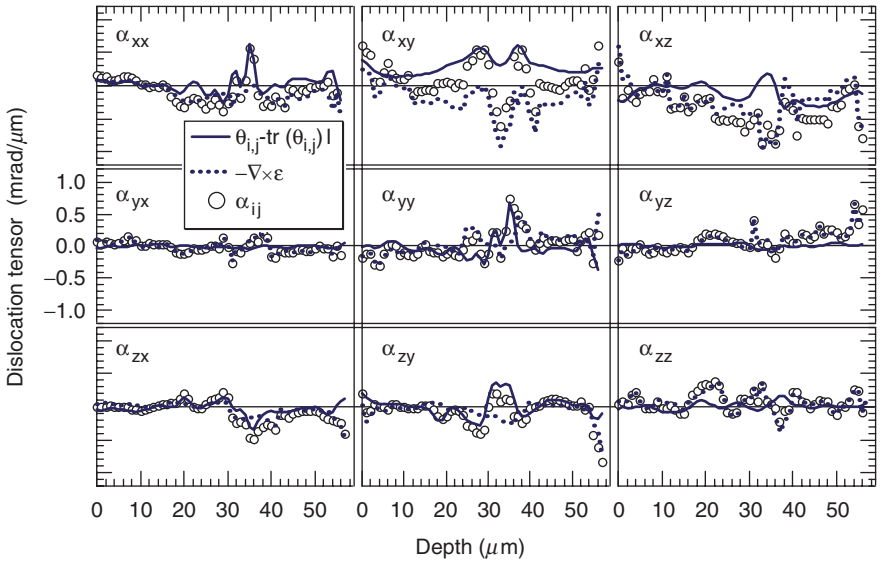

Figure 8. The 3×3 matrix of the dislocation tensors measured along the microbeam for the position in figure 6. Open circles represent the dislocation tensor measurements for micron steps along the beam, the solid line represents the curvature part of the dislocation tensor and the dotted line represents the elastic strain gradient component of the dislocation tensor. Both elastic strain gradient (dashed) and plastic deformation curvature (solid line) effects are presented.

α_{xy} and α_{xz} in figure 8, which are related to gradients of θ_x. Within the measurement fluctuations for this sample, these are the only components with non-zero values over significant distances. Since the curvature (solid lines) and the elastic strains gradients (dotted lines) do not cancel for these α_{ij} components, significant dislocation densities are apparently indicated between depths of 25 and 35 µm by α_{xy} and throughout much of the depth by α_{xz}. Although it is not clear at this point if the non-zero features present at depths of 30–35 µm and near 20 µm in the other components are truly significant, the fact that curvature contributions (solid lines) and elastic strain gradient contributions (dotted lines) are of similar magnitude, in general, indicates that plastic relaxation is not complete in this region and we characterize the elastic and plastic deformation state as mixed. In this connection, it is useful to consider the results in figure 9, where significantly larger curvatures exist as indicated by the curvature measurements in figure 7a.

We note that the magnitude of the $\boldsymbol{\kappa}$ components in figure 9 are at least a factor of 10 larger than in figure 8; moreover, we note that the solid lines and the open circles are approximately equal over most of the range (i.e. $\alpha_{ij} \approx \kappa_{ji} - \delta_{ij}\kappa_{kk}$). The significance of this result is that at this particular sample position (chosen because of the larger rotations and the more complex Laue pattern in figure 4f), the rotational deformation tends to dominate the elastic strain gradients in most places along the measuring line. Considering the difference in scales between figures 8 and 9, the α_{xv} and α_{xz} components are stronger in figure 9 than in figure 8.

Downloaded By: [Oak Ridge National Laboratory] At: 20:52 4 September 2009

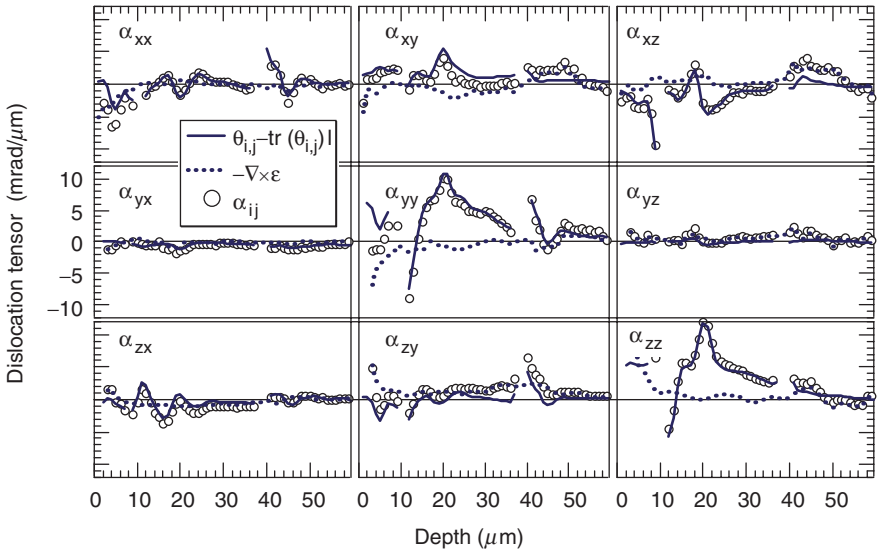

Figure 9. Same as figure 8, but for the second position measured in figure 7 after annealing; the symbols and lines are the same as for figure 8. The elastic strain gradient component (dashed) of the dislocation tensor is negligible compared to the plastic deformation induced curvature (solid line).

However, even larger rotational contributions appear in the α_{yy} and α_{zz} components in figure 9. The structure along the beam for α_{yy} and α_{zz} is very similar because the large peaks present in these two components originate from κ_{xx}, but appear in α_{yy} and α_{zz} by the subtraction of the trace of $\boldsymbol{\kappa}$ in $\alpha_{ij} \approx \kappa_{ji} - \delta_{ij}\kappa_{kk}$. This is a manifestation of the generation of dislocations in the y–z plane by twisting along the x-axis. It also illustrates directly that at this particular measuring position, fluctuations in the dislocation microstructure deviate significantly from cylindrical symmetry along the bend axis.

4. Discussion

The cylindrically bent Si cases considered in figures 5–7 above have been shown to represent three rather different conditions: elastic deformation only in figure 5, both elastic and plastic deformation in figure 6 and largely plastic deformation in figure 7. The elastic deformation case in figure 5 corresponds to the conditions of infinitesimal elastic distortion in section 2.2.3, governed by equation (15), where the rotational, $\mathbf{W}$, and strain, $\boldsymbol{\varepsilon}$, terms are essentially equal and opposite, such that $\boldsymbol{\alpha} = \mathbf{0}$. Figure 6 corresponds to infinitesimal elastic distortion case as well, but in this case, the curvature and elastic strain gradients are not equal in magnitude, so $\boldsymbol{\alpha}$ in figure 8 has non-zero components, α_{xy} and α_{xz}. Figure 7, on the other hand, represents more closely the case of finite rotation with infinitesimal elastic strain

Downloaded By: [Oak Ridge National Laboratory] At: 20:52 4 September 2009

discussed in section 2.2.2, where $\boldsymbol{\alpha} = (\text{curl } \mathbf{R}^{\text{et}})\mathbf{R}^{\text{et}}$ and can be determined to a good approximation from the curvature $\alpha_{\text{ij}} \approx \delta_{\text{ij}}\kappa_{\text{kk}}$ term alone, without measuring the elastic strain. This situation is demonstrated in figure 9, where the strain gradient parts of $\boldsymbol{\alpha}$ (dotted) are negligible compared to the curvature contribution (solid line) parts of $\boldsymbol{\alpha}$. Presently, due to the difficult to quantify uncertainties incurred in measuring elastic strains and strain gradients in the presence of lattice curvature distortions of Laue diffraction peaks, the places in figure 9 in which the strain gradient part of $\boldsymbol{\alpha}$ is large compared to the curvature part may not be significant. To investigate and resolve this issue, the development of methods for deconvoluting rather than simply averaging over distorted Laue diffraction peaks is planned. While this aspect requires further investigation, it is not completely surprising that some experimental and analytical issues remain to be resolved, considering that this is the first time that all nine curvature tensor components and six strain gradient components have been extracted for individual voxels in a plastically deformed material with micron resolution in three dimensions.

With the above caveat, the measured rotations and strain tensors in figures 5–7 and the lattice curvature, strain gradient and dislocation density tensors in figures 8 and 9 illustrate the capability to perform quantitative, three-dimensional, lattice deformation measurements with micron resolution over mesoscopic length scales using 3D X-ray microscopy. Of course, the results presented here provide dislocation tensor components along the microbeam penetration line only, which would not be sufficient for deformation investigations in general. Repeating such measurements over an area (x–y array) would be required for full lattice curvature tensors over entire volumes. However, measurements along single lines suffice for proof-of-principle demonstration purposes of this paper and single lines also made it feasible to show plots of the curvature tensor and deviatoric strain tensor components of $\boldsymbol{\alpha}$ as well as each of the nine components of the dislocation density tensors.

The mrad/μm units on the dislocation density tensor plots emphasize that the individual components represent 'net rotational gradients' generated by the effect of all of the dislocations present in the sample. The nine components of a 3×3 tensor cannot, of course, specify dislocation densities in terms of their slip systems with specific Burgers vectors and dislocation types. For face-centred cubic lattices, for instance, there would be a minimum of 12 edge systems and six screw systems. Rather, the dislocation density tensor quantifies the lattice curvature and elastic strain gradients (with respect to the sample coordinate axes) in terms of the 'effective' dislocation densities required, geometrically, to characterize the crystal incompatibilities within the sample. For comparative purposes, however, we comment that a curvature of $1^\circ/\mu\text{m}$ corresponds to a geometrically necessary dislocation density of $\sim 10^{14}\,\text{m}^{-2}$.

The importance of the dislocation density tensor measurements for fundamental investigations of materials deformation processes is two-fold: they contain detailed, absolute characterizations of the local deformation microstructure (rotational and elastic) within crystalline materials, which can now be measured nondestructively in three dimensions over mesoscopic length scales, and, secondly, this information provides a direct and absolute point of contact between 3D measurements and large-scale computer modelling that either are, or are becoming, capable of detailed

Downloaded By: [Oak Ridge National Laboratory] At: 20:52 4 September 2009

deformation computations on mesoscopic length scales. By convoluting computer simulations with the micron or submicron 3D special resolution of X-ray microscopy measurements it is possible to compare computer simulations of dislocation density tensor components with X-ray microscopy measurements directly on an absolute scale.

Electron backscattering diffraction (EBSD) also provides capabilities to measure rotational deformation and gradients over mesoscopic length scales, and the ability to make elastic strain measurements is becoming possible as well [28–31]. The ease of use and accessibility of EBSD compared to X-ray microscopy is a factor; however, EBSD measurements are inherently 2D, which precludes measurements within bulk samples. For example, the comparison of EBSD and finite element modelling in the investigation of plane strain deformation in a thick, columnar Al tri-crystal [24, 30] was limited to surface deformation measurements even though the computations were performed throughout the sample. This will be an increasingly important issue on the mesoscale, as well as the macroscale, as the capabilities and sophistication of computer simulations and multi-scale modelling continue to increase and poly-crystal, as well as single-crystal materials, are considered in detail. Although 3D measurements with remarkable precision can be performed with EBSD through (destructive) serial-sectioning [31], surface strains and dislocation characteristics may not be fully representative of the bulk before sectioning. Also, angular resolution for EBSD is generally in the order of a few tenths of a degree compared with a few hundredths of a degree for the X-ray measurements discussed here. In general, though, X-ray microscopy and EBSD techniques are complementary and together provide a wide range of capabilities for measuring deformation microstructure, and dislocation density tensors in particular. Moreover, significant advances in spatial resolution, measurement capabilities and availability can be anticipated for the polychromatic techniques discussed here [16, 27] and for monochromatic X-ray techniques [26], as well as for electron scattering techniques.

5. Summary

We have discussed the theoretical basis for the determination of dislocation density tensors on mesoscopic length scales in deformed crystals with references to local lattice curvatures and elastic deformation in the context of 3D X-ray microscopy. Absolute dislocation density tensor measurements have been presented for the case of thin Si plates deformed plastically under cylindrical bending stress at high temperature. Emphasis has been placed on demonstrating measurement techniques and the development of non-destructive methods for determining dislocation density tensors with three-dimensional micron or submicron resolution over mesoscopic length scales in deformed crystalline materials.

Acknowledgements

Research sponsored by the Department of Energy, Office of Science, Division of Materials Sciences at ORNL managed by UT-Battelle, LLC, under contract

Downloaded By: [Oak Ridge National Laboratory] At: 20:52 4 September 2009

DE-AC05-00OR22725. Work was performed on the XOR/UNI Sector 34 ID beamline at the APS; the operation of the APS is sponsored by the DOE. AE was supported by start up funding at Florida State University.

References

[1] L.P. Kubin, in *Materials Science and Technology: A Comprehensive Treatment. Volume 6: Plastic Deformation and Fracture of Materials*, edited by H. Mughrabi (VCH, Weinheim, 1993), p. 137.
[2] L.P. Kubin, in *Stability of Materials*, edited by A. Gonis, P. Turchi and J. Kudrnovsky (Plenum Press, New York, 1996), p. 99.
[3] D.A. Hughes and N. Hansen, Acta Mater. **48** 2985 (2000).
[4] N. Hansen and D.A. Hughes, Phys. Status Solidi (b) **149** 155 (1995).
[5] Q. Liu and N. Hansen, Proc. R. Soc. Lond. A **454** 2555 (1998).
[6] J.F. Nye, Acta Metall. **1** 153 (1953).
[7] E. Kröner, in *Physics of Defects*, edited by R. Balian, M. Kléman and J.-P. Poirier (North-Holland, Amsterdam, 1994), p. 217.
[8] E. Kröner, Int. J. Eng. Sci. **33** 2127 (1995).
[9] B.A. Bilby, R. Bullough and E. Smith, Proc. R. Soc. Lond. A **231** 263 (1955).
[10] K. Kondo, in *RAAG Memoirs of the Unifying Study of Basic Problems in Engineering and Physical Sciences by Means of Geometry*, Volume 1, edited by K. Kondo (Gakujutsu Bunken Fukyu-kai, Tokyo, 1955), p. 459.
[11] P. Cermelli and M. Gurtin, J. Mech. Phys. Solids **49** 1539 (2001).
[12] M.E. Gurtin, J. Mech. Phys. Solids **50** 5 (2002).
[13] M.E. Gurtin, J. Mech. Phys. Solids **52** 2545 (2004).
[14] T. Mura, Phil. Mag. **8** 843 (1963).
[15] E. Kossecka and R. de Wit, Arch. Mech. **29** 749 (1977).
[16] B.C. Larson, W. Yang, G.E. Ice, *et al.*, Nature **415** 887 (2002).
[17] G.E. Ice, B.C. Larson, W. Yang, *et al.*, J. Synchrotron Radiat. **12** 155 (2005).
[18] G.E. Ice and B.C. Larson, Mater. Res. Soc. Bull. **29** 170 (2004).
[19] E. Kröner, Arch. Ration. Mech. Anal. **4** 273 (1969).
[20] F.H. Lee, J. Appl. Mech. **36** 1 (1969).
[21] N. Tamura, J.-S. Chung, G.E. Ice, *et al.*, Mater. Res. Soc. Proc. **563** 175 (1999).
[22] N. Tamura, A.A. MacDowell, R.S. Celestre, *et al.*, Appl. Phys. Lett. **80** 3724 (2002).
[23] J.D. Budai, W. Yang and N. Tamura, Nat. Mater. **2** 487 (2003).
[24] B.C. Larson, W. Yang, J.Z. Tischler, *et al.*, Int. J. Plast. **20** 543 (2004).
[25] W. Yang, B.C. Larson, J.Z. Tischler, *et al.*, Micron **35** 431 (2004).
[26] H.F. Poulsen, *Three-Dimensional X-Ray Diffraction Microscopy* (Springer, Berlin, 2004).
[27] W. Yang, B.C. Larson, G.M. Pharr, *et al.*, J. Mater. Res. **19** 66 (2004).
[28] R.R. Keller, A. Roshko, R.H. Geiss, *et al.*, Microelectron. Eng. **75** 96 (2004).
[29] B.S. El-Dasher, B.L. Adams and A.D. Rollett, Scripta Mater. **48** 141 (2003).
[30] H. Weiland and R. Becker, in *Proceedings of 20th Risø International Symposium on Material Science*, edited by T. Leffer and A.P. Pederson (Risø National Laboratory, Denmark, 1999), p. 213.
[31] N. Zaafarani, D. Raabe, R.N. Singh, *et al.*, Acta Mater. **54** 1863 (2006).

Downloaded By: [Oak Ridge National Laboratory] At: 20:52 4 September 2009